Inorg. Chem. **2008**, *47*, 3669−3678

(TAML)Fe^{IV}=O Complex in Aqueous Solution: Synthesis and Spectroscopic and Computational Characterization

Arani Chanda,[†] Xiaopeng Shan,[‡] Mrinmoy Chakrabarti,[†] W. Chadwick Ellis,[†] Delia L. Popescu,[†] Filipe Tiago de Oliveira,[†] Dong Wang,[‡] Lawrence Que, Jr.,*[,‡] Terrence J. Collins,*[,†] Eckard Münck,*[,†] and Emile L. Bominaar*[,†]

Department of Chemistry, Carnegie Mellon University, Pittsburgh, Pennsylvania 15213, and Department of Chemistry and Center for Metals in Biocatalysis, University of Minnesota, Minneapolis, Minnesota 55455

Received November 21, 2007

Recently, we reported the characterization of the $S = {}^1/_2$ complex $[Fe^V(O)B^*]^-$, where B* belongs to a family of tetraamido macrocyclic ligands (TAMLs) whose iron complexes activate peroxides for environmentally useful applications. The corresponding one-electron reduced species, $[Fe^{IV}(O)B^*]^{2-}$ (**2**), has now been prepared in >95% yield in aqueous solution at pH > 12 by oxidation of $[Fe^{III}(H_2O)B^*]^-$ (**1**), with *tert*-butyl hydroperoxide. At room temperature, the monomeric species **2** is in a reversible, pH-dependent equilibrium with dimeric species $[B^*Fe^{IV}-O-Fe^{IV}B^*]^{2-}$ (**3**), with a pK_a near 10. In zero field, the Mössbauer spectrum of **2** exhibits a quadrupole doublet with $\Delta E_Q = 3.95(3)$ mm/s and $\delta = -0.19(2)$ mm/s, parameters consistent with a $S = 1$ Fe^{IV} state. Studies in applied magnetic fields yielded the zero-field splitting parameter $D = 24(3)$ cm^{-1} together with the magnetic hyperfine tensor $\mathbf{A}/g_n\beta_n = (-27, -27, +2)$ T. Fe K-edge EXAFS analysis of **2** shows a scatterer at 1.69 (2) Å, a distance consistent with a Fe^{IV}=O bond. DFT calculations for $[Fe^{IV}(O)B^*]^{2-}$ reproduce the experimental data quite well. Further significant improvement was achieved by introducing hydrogen bonding of the axial oxygen with two solvent–water molecules. It is shown, using DFT, that the ^{57}Fe hyperfine parameters of complex **2** give evidence for strong electron donation from B* to iron.

1. Introduction

Fe−TAML catalysts (TAML = tetraamido macrocyclic ligand) comprise a family of iron complexes that can activate peroxides to carry out oxidation processes that promise significant environmental impact. To date, they have been demonstrated to be useful, among other things, for destroying trace pollutants in water associated with the textile, pulp and paper, and pesticides industries, for rapidly killing anthrax-like spores and removing sulfur from hydrocarbon fuels.[1,2] The usefulness of Fe−TAML catalysts in a number of practical applications has stimulated us to investigate the chemical basis for their oxidative reactivity.

Because their oxidative potency resembles those of oxygen-activating iron enzymes,[3] it is not surprising that high-valent iron−oxo species immediately come to mind as putative oxidants for Fe−TAML action. Although TAMLs had been shown to support the iron(IV) oxidation state as early as 1990 (reviewed in ref 4), no definitive evidence for iron−oxo species in the TAML family existed until quite recently. The first breakthrough was the crystallographic characterization of two oxo-bridged diiron(IV) complexes that derived from the reaction of dioxygen with their iron(III) precursors in dichloromethane.[5] A second significant achievement was the generation of the first example of an oxo−iron(V) complex, $[Fe^V(O)B^*]^-$ (see Figure 1 for the structure

* To whom correspondence should be addressed. E-mail: que@chem.umn.edu (L.Q.), tc1u@andrew.cmu.edu (T.J.C.), emunck@cmu.edu (E.M.), eb7g@andrew.cmu.edu (E.L.B.).
[†] Carnegie Mellon University.
[‡] University of Minnesota.

(1) Collins, T. J. *Acc. Chem. Res.* **2002**, *35*, 782–790.
(2) Collins, T. J.; Walter, C. *Sci. Am.* **2006**, *294*, 83–90.
(3) Costas, M.; Mehn, M. P.; Jensen, M. P.; Que, L., Jr. *Chem. Rev.* **2004**, *104*, 939–986.
(4) Chanda, A.; Popescu, D.-L.; Tiago de Oliveira, F.; Bominaar, E. L.; Ryabov, A. D.; Münck, E.; Collins, T. J. *J. Inorg. Biochem.* **2006**, *100*, 606–619.
(5) Ghosh, A.; Tiago de Oliveira, F.; Yano, T.; Nishioka, T.; Beach, E. S.; Kinoshita, I.; Münck, E.; Ryabov, A. D.; Horwitz, C. P.; Collins, T. J. *J. Am. Chem. Soc.* **2005**, *127*, 2505–2513.

10.1021/ic7022902 CCC: $40.75
Published on Web 04/02/2008

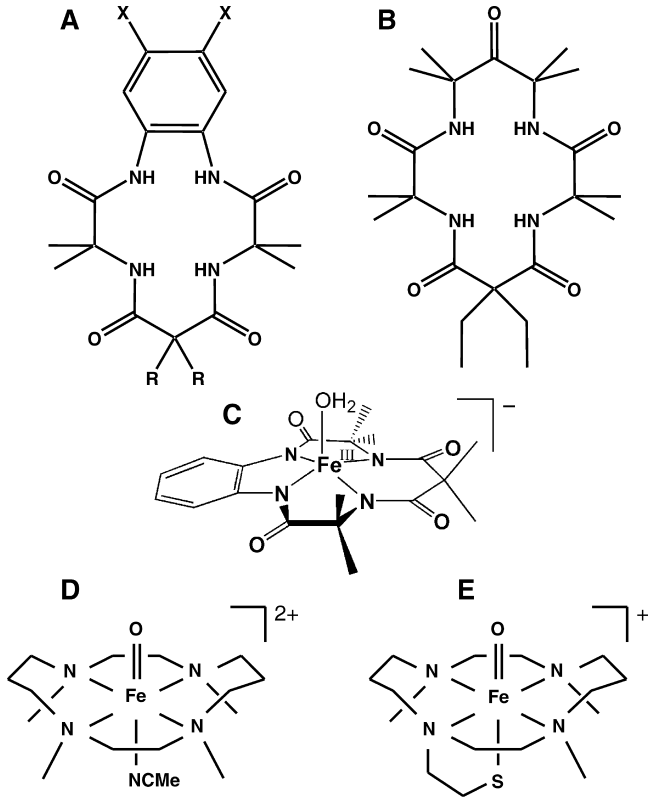

Figure 1. Structures of TAMLs: (A) H_4B^* (R = $-CH_3$, X = $-H$); H_4DCB (R = $-CH_2CH_3$, X = $-Cl$); H_4DMOB (R = $-CH_2CH_3$, X = $-OCH_3$) and (B) H_4MAC^*. Iron complexes with various axial ligands: (C) $[Fe^{III}(H_2O)B^*]^-$ (**1**), (D) $[Fe^{IV}(O)(NCMe)TMC]^{2+}$, and (E) $[Fe^{IV}(O)TMCS]^{2+}$.

of B*), which was obtained in nearly quantitative yield from the reaction of the $[Fe^{III}(H_2O)B^*]^-$, **1**, precursor with peracid in butyronitrile at −60 °C. Under these conditions, $[Fe^{V}(O)B^*]^-$ persisted for hours and was characterized by UV–vis, Mössbauer, EPR, and X-ray absorption spectroscopies.[6]

The iron in $[Fe^{V}(O)B^*]^-$ has a penta-valent oxidation state, unlike compounds **I** of cytochrome P450 and the heme peroxidases, which are best described as iron(IV)−radical species.[7] To obtain the compound **II** analogue, we have turned our attention to the characterization of a species that is present in the room-temperature oxidation chemistry of aqueous Fe^{III}−TAML complexes at high pH. Here, we report the generation of a highly stable $S = 1$ $[Fe^{IV}(O)B^*]^{2-}$, **2**, complex, produced in nearly quantitative yield by reacting **1** with *tert*-butyl hydroperoxide (TBHP) at pH > 12. We have characterized this complex by UV–vis, Mössbauer, and X-ray absorption (XAS) spectroscopies, as well as density functional theory (DFT) calculations. Upon lowering the pH below 12, the Fe^{IV}=O complex was reversibly transformed into the $[B^*Fe^{IV}-O-Fe^{IV}B^*]^{2-}$ dimer, **3**. We thus can describe a series of three high-valent iron−oxo complexes of B* that are inter-related by either one-electron transfer or monomer–dimer reversibility.

The electronic structure of $S = 1$ Fe^{IV}=O species has been the subject of extensive spectroscopic and computational, notably DFT, studies.[8–16] The picture emerging from these efforts is that the two odd electrons of Fe^{IV} are in d_{xz} and d_{yz} orbitals that are substantially admixed with the p_x and p_y orbitals of oxygen. The large spin density at oxygen, resulting from the strong $d_\pi-p_\pi$ interactions, was confirmed by ^{17}O ENDOR of compound **I** of horseradish peroxidase,[8,9] which is an EPR active $S = {}^1/_2$ species because of the antiferromagnetic exchange coupling of the Fe=O moiety to the porphyrin cation radical. An alternative description of the Fe=O bond has been proposed by Girerd and co-workers:[17] on the basis of CASSCF calculations, the Fe=O fragment is formulated as a highly correlated iron(III)−oxyl species. DFT has proven to be a useful tool for predicting the zero-field splitting and hyperfine parameters of high-valent iron complexes.[13,18–20] In this study, this computational technique is applied for identifying **2** as a $S = 1$ Fe^{IV}=O species and elucidating the influence of the strong donor capacity of TAML on the electronic structure parameters obtained from Mössbauer analysis.

2. Materials and Methods

List of Acronyms for Ligands. TMC, 1,4,8,11-tetramethyl-1,4,8,11-tetraaza-cyclotetradecane; TMCS, 2-(4,8,11-trimethyl-1,4,8,11-tetraaza-cyclotetradec-1-yl)-ethanethiol; H_4DCB, 2,3-dichloro-10,10-diethyl-7,7,13,13-tetramethyl-5,7,8,12,13,15-hexahydro-5,8,12,15-tetraaza-benzocyclotridecene-6,9,11,14-tetraone; H_4DMOB, 10,10-diethyl-2,3-dimethoxy-7,7,13,13-tetramethyl-5,7,8,12,13,15-hexahydro-5,8,12,15-tetraaza-benzocyclotridecene-6,9,11,14-tetraone; H_4MAC^*, 6,6-diethyl-3,3,9,9,12,12,14,14-octamethyl-1,4,8,11-tetraaza-cyclotetradecane-2,5,7,10,13-pentaone; and H_4B^*, 7,7,10,10,13,13-hexamethyl-5,7,8,12,13,15-hexahydro-5,8,12,15-tetraaza-benzocyclotridecene-6,9,11,14-tetraone.

Materials. All reagents and solvents were purchased from commercial sources and were used as received, unless noted otherwise. The synthesis of Fe−TAML complexes has been described earlier.[21]

(6) Tiago de Oliveira, F.; Chanda, A.; Banerjee, D.; Shan, X.; Mondal, S.; Que, L., Jr.; Bominaar, E. L.; Münck, E.; Collins, T. J. *Science* **2007**, *315*, 835–838.
(7) Groves, J. T. *J. Inorg. Biochem.* **2006**, *100*, 434–447.
(8) Hanson, L. K.; Chang, C. K.; Davis, M. S.; Fajer, J. *J. Am. Chem. Soc.* **1981**, *103*, 663–670.
(9) Roberts, J. E.; Hoffman, B. M.; Rutter, R.; Hager, L. P. *J. Am. Chem. Soc.* **1981**, *103*, 7654–7656.
(10) Decker, A.; Clay, M. D.; Solomon, E. I. *J. Inorg. Biochem.* **2006**, *100*, 697–706.
(11) Decker, A.; Rohde, J.-U.; Que, L., Jr.; Solomon, E. I. *J. Am. Chem. Soc.* **2004**, *126*, 5378–5379.
(12) Decker, A.; Solomon, E. I. *Angew. Chem., Int. Ed.* **2005**, *44*, 2252–2255.
(13) Schöneboom, J. C.; Neese, F.; Thiel, W. *J. Am. Chem. Soc.* **2005**, *127*, 5840–5853.
(14) Neese, F. *J. Inorg. Biochem.* **2006**, *100*, 716–726.
(15) Conradie, M. M.; Conradie, J.; Ghosh, A. *J. Inorg. Biochem.* **2006**, *100*, 620–626.
(16) Rohde, J.-U.; In, J.-H.; Lim, M. H.; Brennessel, W. W.; Bukowski, M. R.; Stubna, A.; Münck, E.; Nam, W.; Que, L., Jr. *Science* **2003**, *299*, 1037–1039.
(17) Balland, V.; Charlot, M. F.; Banse, F.; Girerd, J. J.; Bill, E.; Bartoli, J. F.; Battioni, P.; Mansuy, D. *Eur. J. Inorg. Chem.* **2004**, 301–308.
(18) Sinnecker, S.; Slep, L. D.; Bill, E.; Neese, F. *Inorg. Chem.* **2005**, *44*, 2245–2254.
(19) Pestovsky, O.; Stoian, S.; Bominaar, E. L.; Shan, X.; Münck, E.; Que, L., Jr.; Bakac, A. *Angew. Chem., Int. Ed.* **2005**, *44*, 6871–6874.
(20) Bukowski, M. R.; Koehntop, K. D.; Stubna, A.; Bominaar, E. L.; Halfen, J. A.; Münck, E.; Nam, W.; Que, L., Jr. *Science* **2005**, *310*, 1000–1002.
(21) Horwitz, C. P.; Ghosh, A. Synthesis patent: US 7060818 B2, **2006**.

Preparation of Samples for Figure 5. Samples for Figure 5 were prepared in two sets. First, 0.5 equiv of TBHP (70% aqueous solution) was added to a 1 mM solution of **1** (as the Na salt) prepared in pH 13 buffer (0.01 M phosphate) to obtain **2**. A total of 100 μL of this solution was added to each of two separate 900 μL buffered solutions of pH 13 and 8.6. Electronic absorption spectra were recorded until a stable absorbance was obtained (dashed lines). In the second set, 0.5 equiv of TBHP were added to a 1 mM solution of **1** prepared at pH 8.6 to obtain **3**. A total of 100 μL of this solution was added to each of two 900 μL buffered solutions of pH 8.6 and 13. Spectra were recorded until a stable absorbance was obtained (solid lines). The spectrum assigned to **3** in Figure 5 differs from that reported in refs 5 and 7. The difference is probably due to the fact that, in this study, **3** was synthesized in water but only to a considerable purity ($\sim$ 80%), leaving some residual absorbance of **1** in the 365–400 nm region of Figure 5. The electronic absorption spectrum of **1** is strongly dependent upon pH and has a band at 365 nm that vanishes at pH > 12, making the UV spectral region less suitable for the analysis of the dimer−monomer conversion. Furthermore, the change in solvent may also have played some role in terms of the extinction coefficient.

Preparation of Samples for Mössbauer and XAS Studies. A typical preparation of ^{57}Fe-enriched complex **2** was performed as follows. A 0.5–1 mL solution of ^{57}Fe-enriched **1** (1–2 mM) in 1 M KOH solution was placed into an optical cuvette at room temperature. A half equiv of TBHP solution was added and mixed promptly. The reaction was followed by UV–vis spectrometry until the 435 nm band reached a maximum, indicating the complete formation of **2**. Solutions were taken out directly from the UV–vis cuvettes to Mössbauer/EXAFS cups and frozen in liquid nitrogen.

Preparation of Samples for Figure 7. First, a stock solution of **1** (1 mM) was prepared in water. Each time 100 μL of this solution was then added to 900 μL of 0.01 M phosphate buffer of pH 8.6, 9.0, 9.5, 10.0, 10.5, 11.0, 11.5, and 12.0, respectively. The accuracy of the pH measurements was $\pm$0.1 units. To each of these 0.1 mM solutions of **1**, 0.5 equiv of TBHP was added and electronic absorption spectra were recorded until a steady absorbance was reached (10–15 min).

Spectroscopy. UV–vis spectrophotometric measurements were performed using a Hewlett-Packard diode array spectrophotometer (model 8453) equipped with a thermostatted cell holder and an automated 8-cell positioner. A thermo digital temperature controller RTE17 was employed to control the temperature to within an accuracy of $\pm$1 °C. Both quartz and appropriate plastic cuvettes of different path lengths were used.

Mössbauer spectra were recorded with two spectrometers using Janis Research, Inc., SuperVaritemp dewars that allow studies in applied magnetic fields up to 8.0 T in the temperature range from 1.5 to 200 K. Spectral simulations were performed using the WMOSS software package (WEB Research, Minneapolis, MN). Isomer shifts are quoted relative to Fe metal at 298 K.

XAS Analysis of [Fe^{IV}(O)B*]$^{2-}$. Fe K-edge X-ray absorption spectra (XAS, fluorescence excitation, Ge detector) were recorded on frozen aqueous solutions at 10(1) K over the energy range of 6.9–8.0 keV. The monochromator was calibrated using the K-edge energy of iron foil at 7112.0 eV (beamline 7-3 at SSRL, Stanford Synchrotron Radiation Laboratory). The program EXAFSPAK[22] was used for evaluation, calibration, and summation of the data, and the program SSExafs[23,24] was used for analysis of pre-edge and EXAFS regions. The edge energy E_0 has been determined by taking the first inflection point of the first derivative of the spectra, representing the transition of a 1s electron to the continuum. A back-transformation range $r' = 0.40-3.10$ Å was used for fitting the EXAFS data; however, a fit to unfiltered data (fit 7 in Table 2) corresponding to the best fit to filtered data (fit 6 in Table 2) showed no significant difference.

DFT Calculations. The DFT calculations were performed with Becke's three-parameter hybrid functional (B3LYP)[25,26] and basis set 6-311G provided by the Gaussian 03 (release C.02) software package.[27] The results of the calculations and derived quantities for [Fe^{IV}(O)B*]$^{2-}$ are summarized in Figure 8 and Tables S1–S3 in the Supporting Information. Geometry optimizations were performed for the $S = 0$, 1, and 2 states of [Fe(O)B*]$^{2-}$ and terminated upon reaching the default convergence criteria. The equilibrium conformation for $S = 1$ (Figure 8) has the lowest energy, in agreement with the triplet ground state observed for complex **2**. The optimizations did not impose any symmetry. The frequencies for the equilibrium conformation obtained with the FREQ keyword are all positive, indicating the identification of a minimum. Time-dependent (TD) DFT calculations for the $S = 1$ SCF solution gave exclusively positive excitation energies, confirming that the SCF solution represents the ground state. The "vertical" excitation energies, obtained for the equilibrium geometry of the $S = 1$ ground state, which contribute to the zero-field splitting are summarized in Table S1 in the Supporting Information. The principal values, $V_{\xi\xi}$, of the EFG tensor [from which the quadrupole splitting and asymmetry parameter were obtained using the expressions $\Delta E_Q = (eQ/2)V_{zz}(1 + \eta^2/3)^{1/2}$ and $\eta = (V_{xx} - V_{yy})/V_{zz}$] and tensor $\mathbf{A}^{SD}$ (SD = spin dipolar) were calculated with the PROPERTIES keyword. The EFG components were converted from atomic units to mm s^{-1} by the multiplication with -1.6 mm s^{-1}/AU (Tables 1 and 3). In Figure 10, we have used a slightly smaller conversion factor, -1.43 mm s^{-1}/AU. For this value, the slope of the linear regression analysis of the correlation between the experimental and calculated ΔE_Q values for the Fe^{III}, Fe^{IV}, and Fe^{V} complexes is equal to 1.[28] The calculated isomer shifts, δ, were obtained from

(22) George, G. N. EXAFSPAK, Stanford Synchrotron Radiation Laboratory, Stanford Linear Accelerator Center, 1990.

(23) Scarrow, R. C.; Maroney, M. J.; Palmer, S. M.; Roe, A. L.; Que, L., Jr.; Salowe, S. P.; Stubbe, J. *J. Am. Chem. Soc.* **1987**, *109*, 7857–7864.

(24) Scarrow, R. C.; Trimitsis, M. G.; Buck, C. P.; Grove, G. N.; Cowling, R. A.; Nelson, M. J. *Biochemistry* **1994**, *33*, 15023–15035.

(25) Becke, A. D. *J. Chem. Phys.* **1993**, *98*, 5648.

(26) Lee, C.; Yang, W.; Parr, R. G. *Phys. Rev. B: Condens. Matter Mater. Phys.* **1988**, *37*, 785.

(27) Frisch, M. J.; Trucks, G. W.; Schlegel, H. B.; Scuseria, G. E.; Robb, M. A.; Cheeseman, J. R.; Montgomery, J. A. J.; Vreven, T.; Kudin, K. N.; Burant, J. C.; Millam, J. M.; Iyengar, S. S.; Tomasi, J.; Barone, V.; Mennucci, B.; Cossi, M.; Scalmani, G.; Rega, N.; Petersson, G. A.; Nakatsuji, H.; Hada, M.; Ehara, M.; Toyota, K.; Fukuda, R.; Hasegawa, J.; Ishida, M.; Nakajima, T.; Honda, Y.; Kitao, O.; Nakai, H.; Klene, M.; Li, X.; Knox, J. E.; Hratchian, H. P.; Cross, J. B.; Bakken, V.; Adamo, C.; Jaramillo, J.; Gomperts, R.; Stratmann, R. E.; Yazyev, O.; Austin, A. J.; Cammi, R.; Pomelli, C.; Ochterski, J. W.; Ayala, P. Y.; Morokuma, K.; Voth, G. A.; Salvador, P.; Dannenberg, J. J.; Zakrzewski, V. G.; Dapprich, S.; Daniels, A. D.; Strain, M. C.; Farkas, O.; Malick, D. K.; Rabuck, A. D.; Raghavachari, K.; Foresman, J. B.; Ortiz, J. V.; Cui, Q.; Baboul, A. G.; Clifford, S.; Cioslowski, J.; Stefanov, B. B.; Liu, G.; Liashenko, A.; Piskorz, P.; Komaromi, I.; Martin, R. L.; Fox, D. J.; Keith, T.; Al-Laham, M. A.; Peng, C. Y.; Nanayakkara, A.; Challacombe, M.; Gill, P. M. W.; Johnson, B.; Chen, W.; Wong, M. W.; Gonzalez, C.; Pople, J. A. Gaussian, Inc., Wallingford CT, 2004.

(28) In earlier reports, we used the factor -1.6 mm s^{-1}/AU. The set of high-oxidation complexes considered here require a slightly smaller factor. As for the isomer shift, the calibration constant for the quadrupole splitting depends upon the basis set and functional and is considered here as a semi-empirical parameter.

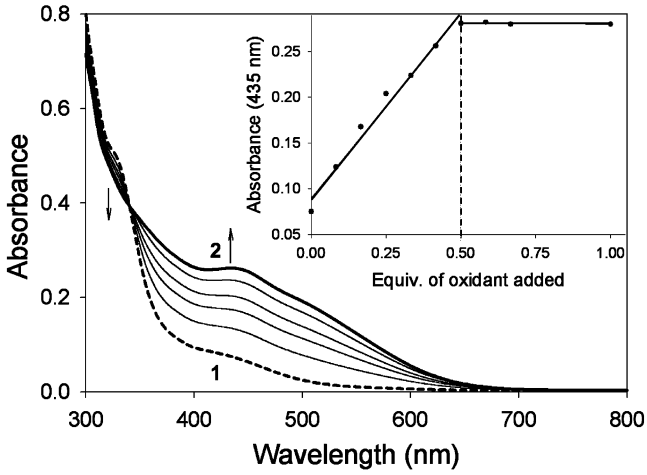

Figure 2. Formation of **2** (bold solid line) from **1** (dashed line) by addition of 0.5 equiv of TBHP, at pH 14, over a time period of ~10 min. Inset shows the changes in absorption at 435 nm as a function of the number of TBHP equivalents added.

the electron density at the iron nucleus using the calibration of Vrajmasu et al.[29] The calibration constants essentially depend upon the choice of the basis set and the functional. Other calibrations for the isomer shift can be found in refs 18 and 30–35. The DFT values for the Mössbauer parameters in Table S3 in the Supporting Information were evaluated for optimized geometries. The DFT results for δ and ΔE_Q for the complexes of Figures 9 and 10 and Table 3 were obtained as described above for $[Fe^{IV}(O)B^*]^{2-}$.

3. Results and Discussion

3.1. Electronic Absorption and Mössbauer Studies. The addition of *tert*-butyl hydroperoxide (TBHP) to an aqueous solution of $Na[Fe^{III}(H_2O)B^*]$ (**1**), prepared in 0.1 M KOH solution (or 0.1 M phosphate buffer of pH 13.7), generates a red species (**2**, λ_{max} = 435 nm; Figure 2). Species **2** is quite stable at room temperature, decaying by less than 10% in 2 h. A titration of **1** with TBHP revealed that ca. 0.5 equiv of oxidant per Fe^{III} is required to obtain the maximum yield of **2** (inset in Figure 2), indicating the formation of a Fe^{IV} species. A one-to-one transformation of **1** to **2** is indicated by an isosbestic point at 350 nm. Quantitation of **2** by Mössbauer spectroscopy (see below) yielded the extinction coefficient ε_{435} = 2500(200) M^{-1} cm^{-1}.

We have studied samples of **2** with Mössbauer spectroscopy between 4.2 and 140 K in applied magnetic fields up to 8.0 T. Three representative spectra are shown in Figure 3. In zero field, complex **2** exhibits a doublet with quadrupole splitting, ΔE_Q = 3.95(3) mm/s, and isomer shift, δ = −0.19(2) mm/s. As shown below in the discussion of Figures

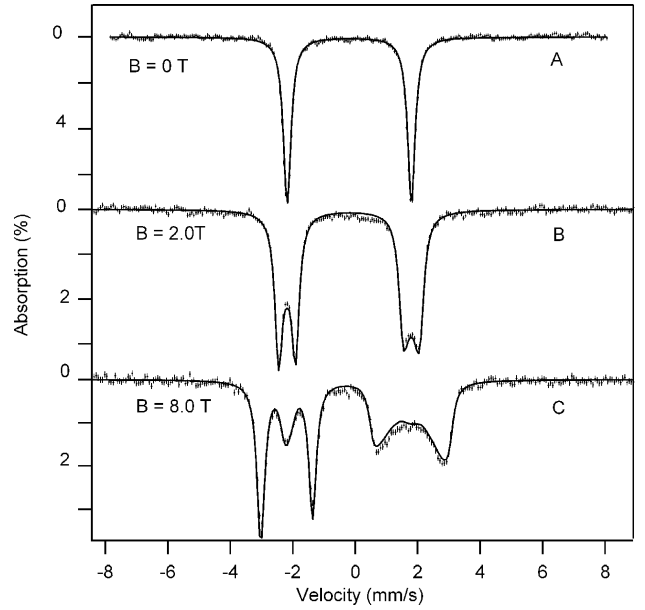

Figure 3. Mössbauer spectra (4.2 K) of **2** in aqueous solution, at pH 14, recorded in parallel-applied fields 0 T (A), 2.0 T (B), and 8.0 T (C). The solid lines are spectral simulations based on eq 1 using the parameters listed in Table 1. At least 95% of the iron in the sample belongs to **2**.

9 and 10, these parameters are characteristic of S = 1 Fe^{IV}−TAML complexes. We have analyzed the applied field spectra with the S = 1 spin Hamiltonian

$$H = D(\hat{S}_z^2 - 2/3) + E(\hat{S}_x^2 - \hat{S}_y^2) + \beta\hat{\mathbf{S}}\cdot\mathbf{g}\cdot\mathbf{B} + \hat{\mathbf{S}}\cdot\mathbf{A}\cdot\hat{\mathbf{I}} - g_n\beta_n\mathbf{B}\cdot\hat{\mathbf{I}} + (eQV_{zz}/12)[3\hat{I}_z^2 - 15/4 + \eta(\hat{I}_x^2 - \hat{I}_y^2)] \quad (1)$$

where D and E are zero-field splitting (ZFS) parameters, **B** is the applied magnetic field, I is the nuclear spin of ^{57}Fe, and **A** is the magnetic hyperfine tensor. The solid lines in Figure 3 are spectral simulations (to a set of eight spectra) based on eq 1, using the parameters listed in Table 1. Similar to most S = 1 Fe^{IV} complexes,[19,20,36] **2** exhibits a large and positive zero-field splitting, D = 24(3) cm^{-1}. Neese and coworkers[13,14] and others[19,20] have ascribed the large D values to contributions arising from spin–orbit coupling of the S = 1 ground state with excited S = 2 and S = 0 states. In section 3.4.4, the contributions to D from S = 0, 1, and 2 are estimated for complex **2**. If the coupling of the ground state with S = 1 states from the t_{2g} manifold provides a significant contribution to D, there is an attendant reduction in the magnitude of the x and y components of the **A** tensor and an increase in g_x and g_y.[37] In contrast, the spin–orbit coupling of the S = 1 ground state with S = 2 and S = 0 excited states, while contributing to D, has no first-order effect on **g** and **A**.[38] The x and y components of **A** listed in Table 1 are among the largest in magnitude observed for S = 1 Fe^{IV} complexes; below, we will rationalize this observation. The Mössbauer parameters of **2** establish this complex as a S = 1 Fe^{IV} species.

(29) Vrajmasu, V.; Münck, E.; Bominaar, E. L. *Inorg. Chem.* **2003**, *42*, 5974–5988.
(30) Nieuwpoort, W. C.; Post, D.; Duijnen, P. T. *Phys. Rev. B: Condens. Matter Mater. Phys.* **1978**, *17*, 91–98.
(31) Reschke, R.; Trautwein, A. X.; Desclaux, J. P. *J. Phys. Chem. Solids* **1977**, *38*, 837–841.
(32) Han, W. G.; Liu, T.; Lovell, T.; Noodleman, L. *J. Comput. Chem.* **2006**, *27*, 1292–1306.
(33) Liu, T.; Lovell, T.; Han, W. G.; Noodleman, L. *Inorg. Chem.* **2003**, *42*, 5244–5251.
(34) Zhang, Y.; Mao, J.; Oldfield, E. *J. Am. Chem. Soc.* **2002**, *124*, 7829–7839.
(35) Neese, F. *Inorg. Chim. Acta* **2002**, *337C*, 181–192.
(36) Lim, M. H.; Rohde, J.-U.; Stubna, A.; Bukowski, M. R.; Costas, M.; Ho, R. Y. N.; Münck, E.; Nam, W.; Que, L., Jr. *Proc. Nat. Acad. Sci. U.S.A.* **2003**, *100*, 3665–3670.
(37) Oosterhuis, W. T.; Lang, G. *J. Chem. Phys.* **1973**, *58*, 4757–4765.
(38) Neese, F.; Solomon, E. I. *Inorg. Chem.* **1998**, *37*, 6568–6582.

Table 1. Experimental[a] and Calculated[b] Fine Structure and Hyperfine Parameters for Complex **2**

method	δ (mm/s)	ΔE_Q (mm/s)	η	A_x (T)	A_y (T)	A_z (T)	$g_\perp$	g_Δ	D (cm^{-1})	E/D
experimental	−0.19(2)	3.95(3)	0	−27(3)	−27(3)	+2(3)	∼2	∼2	24(3)	∼0
calculated	−0.12[c]	3.5[c]	0	−24.9	−24.6	−0.5	1.96	2.00	26.5	∼0

[a] From Mössbauer analysis. [b] From DFT calculations for $[Fe^{IV}(O)B^*]^{2-}$ in the gas phase. See section 2 for details. [c] These values change to −0.14 and 4.0 mm/s when the axial oxygen is hydrogen-bonded to water molecules of the solvent. See the text for details.

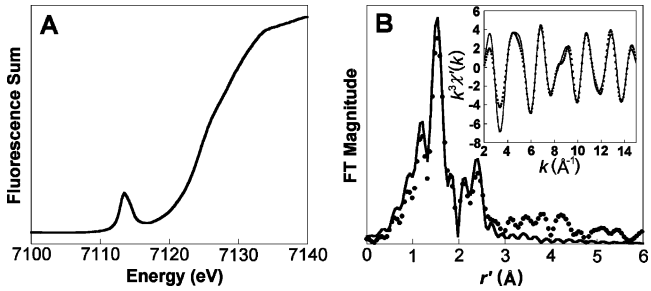

Figure 4. (A) Fe K-edge X-ray absorption near-edge structure (XANES, fluorescence excitation) of $[Fe^{IV}(O)B^*]^{2-}$ (**2**). (B) Fourier transform of the Fe K-edge EXAFS data ($k^3\chi(k)$) and Fourier-filtered EXAFS spectra ($k^3\chi'(k)$, inset) for $[Fe^{IV}(O)B^*]^{2-}$ (**2**). Fourier transform range $k = 2-15$ Å^{-1}; back-transform range $r' = 0.40-3.10$ Å; fit with parameters listed in fit 6 in Table 2. Dots, experimental data; solid lines, fits.

Table 2. EXAFS Fitting Results for $[Fe^{IV}(O)B^*]^{2-}$ (**2**)[a]

	Fe−O			Fe−N			Fe···C			GOF
fit	n	r (Å)	$\Delta\sigma^2$	n	r (Å)	$\Delta\sigma^2$	n	r (Å)	$\Delta\sigma^2$	ε^2 10^3
1				6	1.90	4.4				1.52
2				5	1.90	2.6				1.30
3	1	1.68	−0.4	5	1.89	2.4				1.04
4	1	1.70	1.1	4	1.90	0.8				0.93
5	1	1.68	−0.3	5	1.89	2.5	5	2.84	2.9	0.83
6	1	1.69	1.2	4	1.90	0.9	5	2.84	3.2	0.64[b]
7	1	1.70	1.7	4	1.90	0.8	5	2.83	3.1	1.25[c]

[a] Fourier transform range $k = 2-15$ Å^{-1}; back-transformation range $r' = 0.40-3.10$ Å. n is the coordination number for a particular scatterer (O, N, or C). r is its distance from the iron center. $\Delta\sigma^2$ is the Debye–Waller factor. GOF is the EXAFS goodness of fit criterion, with $\varepsilon^2 = [(N_{idp}/\nu)\Sigma(\chi_c - \chi)^2/\sigma_{data}^2]/N$. [b] Best fit. [c] Fit to unfiltered data corresponding to the best fit to filtered data.

3.2. XAS Studies. Information about the structural nature of **2** is obtained from X-ray absorption spectroscopic studies at the Fe K edge (Figure 4). A sample in frozen aqueous solvent, more than 90% pure in **2** according to Mössbauer spectroscopy, exhibits a K edge at 7124.5 eV, which is 0.6 eV higher than the K edge for $[Fe^{III}(H_2O)B^*]^-$ and 0.8 eV lower than the edge for $[Fe^{V}(O)B^*]^-$.[6] Similarly, the pre-edge peak of **2** at 7113.5 eV is found to be 0.5 eV higher than that of $[Fe^{III}(H_2O)B^*]^-$ and 0.6 eV lower than that of $[Fe^{V}(O)B^*]^-$.[6] These observations support the Mössbauer assignment that **2** is a Fe^{IV} complex. The 1s → 3d pre-edge transition found for **2** is rather intense, with an area of 41 units (Figure 4A), which is halfway in between the values of 17 units for $[Fe^{III}(H_2O)B^*]^-$ and 60 units for $[Fe^{V}(O)B^*]^-$. The pre-edge peak area of **2** is larger than any observed to date for $S = 1$ oxo−iron(IV) species, the areas of which range from 18 to 38 units.[20,39]

Direct evidence that **2** is a Fe^{IV}=O complex was obtained from the analysis of the EXAFS region of the X-ray absorption spectrum (Figure 4B). The best fit obtained consisted of three shells, namely, one O scatterer at 1.69 Å, four N/O scatterers at 1.90 Å, and five C scatterers at 2.84 Å (Table 2). The scatterers at 1.90 and 2.84 Å are consistent with low Z atoms of the macrocyclic ligand as found in the EXAFS fits for $[Fe^{III}(H_2O)B^*]^-$ and $[Fe^{V}(O)B^*]^-$ complexes; the coordination number of the C shell is lower than the expected value of 8 because of the distribution of Fe···C distances, which differ by as much as 0.12 Å in the crystal structure of the (μ-oxo)diiron(IV)−TAML complex.[5] Most importantly, the 1.69 Å scatterer can be assigned to the oxo atom of a Fe−O unit, with a distance that is 0.10 Å longer than obtained for the $[Fe^{V}(O)B^*]^-$ complex[6] but 0.04 Å shorter than the Fe−O distance obtained in the crystal structure of the (μ-oxo)diiron(IV)−TAML complex.[5]

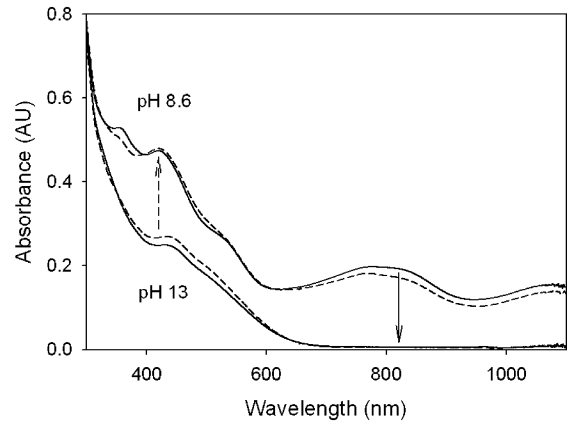

Figure 5. Solid lines show the change in UV–vis spectral pattern in changing the pH from 8.6 to 13 (solid arrow). Dashed lines shows transformation of **2** to **3** as the pH is changed from 13 to 8.6 (see the Materials and Methods).

3.3. pH Dependence. To assess the pH range of the stability of complex **2**, we have conducted electronic absorption spectroscopy and Mössbauer studies between pH 14 and 8.6. When the pH of a preformed solution of **2** was changed from pH 13 to 8.6 (10 mM phosphate buffer), significant changes in the electronic absorption spectrum occurred instantly (<1 s). The new species (Figure 5) exhibits a spectral pattern similar to that for the μ-oxo-bridged $[B^*Fe^{IV}-O-Fe^{IV}B^*]^{2-}$ species, **3**, reported by Ghosh et al.[5] Figure 6A shows a 4.2 K Mössbauer spectrum recorded after freezing a TBHP-oxidized sample prepared at pH 8.6. The spectrum exhibits a doublet (ca. 75% of Fe) with $\Delta E_Q = 3.25(3)$ mm/s and $\delta = -0.07(2)$ mm/s. These parameters are essentially identical to those reported for the diamagnetic $Fe^{IV}-O-Fe^{IV}$ complex, **3** ($\Delta E_Q = 3.3$ mm/s, $\delta = -0.07$ mm/s, observed in the solid and in acetonitrile). Studies in strong applied magnetic fields (not shown) demonstrate that the $\Delta E_Q = 3.25$ mm/s species observed here is indeed diamagnetic, in support of assigning this doublet to **3**. The pH 8.6 sample exhibits a second doublet with $\Delta E_Q = 4.7$ (1) mm/s and $\delta = -0.20(4)$ mm/s that represents ca. 12%

(39) Rohde, J.-U.; Torelli, S.; Shan, X.; Lim, M. H.; Klinker, E. J.; Kaizer, J.; Chen, K.; Nam, W.; Que, L., Jr. *J. Am. Chem. Soc.* **2004**, *126*, 16750–16761.

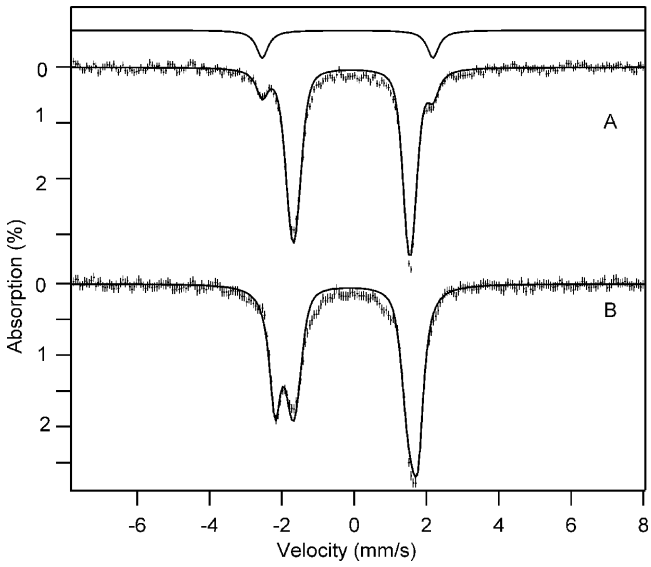

Figure 6. Zero-field 4.2 K Mössbauer spectra of **1** oxidized with TBHP at pH 8.6 (A) and pH 11.7 (B). The major doublet in A, accounting for ~76% of Fe, belongs to $[B^*Fe^{IV}-O-Fe^{IV}B^*]^{2-}$, **3**. A second doublet (drawn separately above the data, ~12%) with $\Delta E_Q = 4.7(1)$ mm/s and $\delta = -0.20$ (4) mm/s belongs to an as yet unidentified Fe^{IV} species. (B) Sample was prepared at pH 11.7 and then frozen by immersion into liquid nitrogen. The solid line is a superposition of two doublets belonging to mononuclear complex **2** (46%) and dimer **3** (43%).

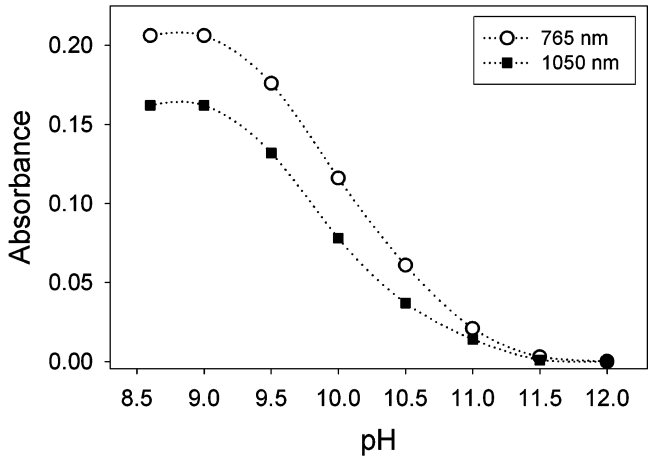

Figure 7. Plot of the absorbance at 765 and 1050 nm, bands assigned to $[B^*Fe^{IV}-O-Fe^{IV}B^*]^{2-}$, as a function of pH (see the Materials and Methods).

of the Fe in the sample (spectrum drawn to scale above the data of Figure 6A). This species, on the basis of the isomer shift and the observation of a doublet in zero applied field, is an Fe^{IV} complex of unidentified nature. The sample also contains a minor paramagnetic component with unresolved features. EPR studies (not shown) suggest that this component belongs to a $Fe^{III}Fe^{IV}$ dimer (This complex presently is being studied in the laboratories of T. J. Collins and M. P. Hendrich at Carnegie Mellon University).

Figure 7 shows a plot of the absorbance at 765 and 1050 nm (bands assigned to **3**) as a function of pH. This titration indicates a pK_a near 10. However, a Mössbauer sample prepared at pH 11.7 exhibits two doublets (Figure 6B), belonging to **2** (46%) and **3** (43%). A study of the pH dependence with Mössbauer spectroscopy (in frozen solution) showed the transition between **2** and **3** to be compressed into a narrow pH range of 11.6–11.9. We suspect that pH changes of the phosphate buffer upon freezing[40,41] are responsible for the different behavior observed between room-temperature electronic absorption and frozen solution Mössbauer studies.

Table 3. Influence of Axial Ligands in $[Fe^{IV}(X)(Y)B^*]^{n-}$ (X/Y = O, −OH, and H_2O) on Isomer Shift δ, Quadrupole Splitting ΔE_Q, and Fe−O Distance[a]

Fe^{IV} Model Complex	δ (mm/s)	ΔE_Q (mm/s)	Fe–O (Å)
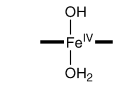	−0.11	5.1	1.80,‡ 2.27‡
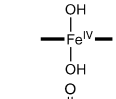	−0.15	3.6	1.88‡, 1.88‡
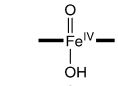	−0.07‡	1.6‡	1.69, 2.05‡
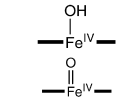	−0.07‡	4.4	1.80‡
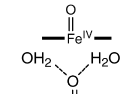	−0.12	3.5	1.65
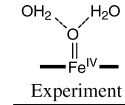	−0.14	4.0	1.68
Experiment	−0.19(2) [c]	3.95(3) [c]	1.69(2) [d]

[a] Properties obtained by DFT calculations for the geometry-optimized structure in the $S = 1$ state. [b] Two water molecules are hydrogen-bonded to axial oxygen; see Figure S1 in the Supporting Information for the optimized structure. [c] From Mössbauer analysis. [d] From EXAFS analysis. ‡ Violates one of the three conditions given in the text.

We thus have in hand two iron(IV)−oxo complexes of B* that can be inter-related by a pH equilibrium. Starting from **3**, complex **2** can be formed by increasing the pH to above 12. This transformation can be reversed by lowering the pH. $[Fe^{IV}(O)B^*]^{2-}$ in turn is in principle related to $[Fe^{V}(O)B^*]^{-}$ by one-electron transfer. However, the different solvent conditions under which these two complexes are generated hamper efforts to establish this relationship. For example, the highly basic aqueous conditions needed to generate and stabilize $[Fe^{IV}(O)B^*]^{2-}$ give rise to background signals in the cyclic voltammetric scans that potentially obscure the anticipated $Fe^{V/IV}$ wave. As an alternative strategy, we attempted chemical reductions of $[Fe^{V}(O)B^*]^{-}$ and found that this complex can be reduced by dicacetylferrocene ($E_{1/2} = 490$ mV versus Fc) in acetonitrile to afford the (μ-oxo)diiron(IV) complex, **3**. Presumably, electron transfer to $[Fe^{V}(O)B^*]^{-}$ initially forms $[Fe^{IV}(O)B^*]^{2-}$, which because of its high basicity readily acquires a proton from the solution and converts to the dimer.[5] This result allows us to estimate the $Fe^{V/IV}$ potential to be greater than 490 mV versus Fc. This value is not unreasonable, considering the reported electrochemistry of $[B^*Fe^{IV}-O-Fe^{IV}B^*]^{2-}$ that shows a one-electron reduction at −230 mV versus Fc ($Fe^{IV}Fe^{IV}/Fe^{III}Fe^{IV}$) and two one-electron oxidations at +370 and +720 mV (formally $Fe^{V}Fe^{IV}/Fe^{IV}Fe^{IV}$ and $Fe^{V}Fe^{V}/Fe^{IV}Fe^{V}$, respectively).[5]

(40) Pikal-Cleland, K. A.; Rodriguez-Horendo, N.; Godon, A.; Carpenter, J. F. *Arch. Biochem. Biophys.* **2000**, *384*, 398–406.
(41) Gomez, G.; Pikal, M. J.; Rodriguez-Horendo, N. *Pharm. Res.* **2001**, *18*, 90–97.

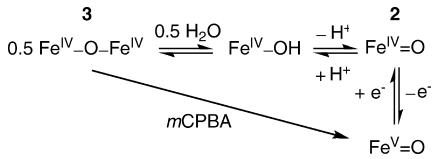

The properties of [B*Fe^{IV}−O−Fe^{IV}B*]$^{2-}$ (**3**), [Fe^{IV}(O)-B*]$^{2-}$ (**2**), and [Fe^{V}(O)B*]$^{-}$ characterized to date should allow us to assess the roles of these high-valent Fe−B* species in the complex reactivity profile for the numerous demonstrated catalytic transformations with tightly pH-determined interrelationships.

3.4. DFT Calculations. 3.4.1 Axial Coordination. To assess the axial coordination of **2**, we have conducted DFT calculations for a series of plausible axial ligands. These formulations of the complex have been listed in Table 3, together with the DFT values for the ^{57}Fe isomer shifts, quadrupole splittings, and Fe−O distances predicted for the species. The obvious candidate, [Fe^{IV}(O)(H$_2$O)B*]$^{2-}$, has not been listed because the axial water molecule dissociates in the course of the geometry optimization.

The parameter values calculated for the species of Table 3 can be compared to the experimental data for complex **2** listed at the bottom of the table. Our DFT experience with TAML complexes suggests that, for an acceptable description of **2**, the parameters should roughly satisfy the following conditions: $|\delta - \delta_{exp}| < 0.08$ mm/s, $|\Delta E_Q - \Delta E_{Q,exp}| < 1.0$ mm/s, and bond-length difference $|(Fe-O) - (Fe-O)_{exp}| < 0.05$ Å. Entries in the table that violate one of the conditions are marked (‡). The table shows that complexes with axial ligands other than O have at least one parameter outside the specified range. We conclude from this result that spectroscopic species **2** is the intermediate-spin ($S = 1$) five-coordinate complex [Fe^{IV}(O)B*]$^{2-}$. A picture of the geometry-optimized structure of the complex is shown in Figure 8.

The gas-phase value for [Fe^{IV}(O)B*]$^{2-}$, $\delta = -0.12$ mm/s, is 0.07 mm/s larger than the experimental target. The agreement is not quite satisfactory but is slightly improved when the axial oxygen is hydrogen-bonded to two water molecules (seventh row of Table 3), obtaining $\delta = -0.14$ mm/s. The hydrogen bonding further improves the agreement of the calculated values for ΔE_Q and the Fe−O distance with the experimental data. The Fe−O bond length increases by 0.03 Å under the influence of the two water molecules and is within the error margin equal to the value deduced from the EXAFS data [1.69(2) Å]. The calculated isomer shift of the new species is halfway between the values found for Fe^{III}− and Fe^{V}−TAML complexes and supports the identification of **2** as a Fe^{IV} species. The value calculated for the quadrupole splitting of **2** gives a large, positive value, which distinguishes it from the $\Delta E_Q = 0.89$ mm/s ($D = -2.6$ cm^{-1}) of the only known $S = 2$ Fe^{IV}−TAML complex, [Fe^{IV}(Cl)MAC*]$^{-}$. In the following sections, we discuss the electronic structure of **2**, on the basis of a comparison of the spectroscopic observables for **2** with those for other Fe^{IV} species.

3.4.2 Isomer Shift. In the past 3 years, we have studied a variety of Fe^{IV} complexes, experimentally as well as theoretically.[4–6,19,20] Nonheme Fe^{IV}=O complexes are now available for three equatorial ligand combinations with

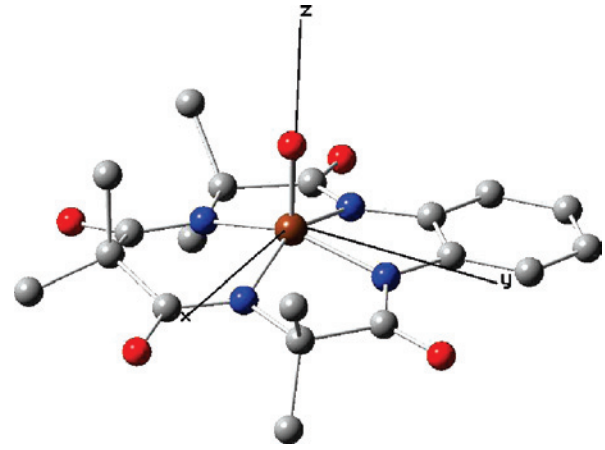

Figure 8. Geometry-optimized structure of **2** in the gas phase as obtained from DFT calculations for the $S = 1$ ground state. Color code: brown, iron; red, oxygen; blue, nitrogen; and gray, carbon. Hydrogen atoms are not shown for clarity. Selected bond lengths: Fe−O, 1.65 Å; (Fe−N)$_{av}$, 1.915 Å; the Fe is 0.44 Å above the plane defined by the four amide nitrogens. The Cartesian axes used in the discussion have been indicated. For the structure including hydrogen bonding to two water molecules, see Figure S1 in the Supporting Information.

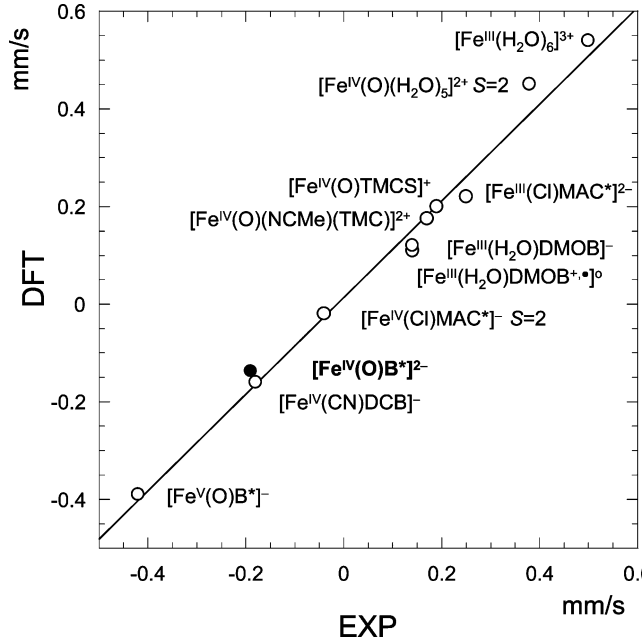

Figure 9. Correlation between DFT calculated and experimental isomer shifts for three different ligand systems.[4,6,19,20] TAML complexes are listed to the right of the regression line. The correlation coefficient R^2 is 0.99. Complex **2** is indicated with a solid dot.

widely differing donor strengths; weak, medium, and strong nonoxo donors are found in [Fe^{IV}(O)(H$_2$O)$_5$]$^{2+}$,[19] [Fe^{IV}(O)-(MeCN)TMC]$^{+}$,[20] and [Fe^{IV}(O)B*]$^{2-}$, respectively. The increasing ligand field in the series causes a steep rise in the energy of the x^2-y^2 orbital and transforms the orbital configuration (spin) $(xy)^1(xz)^1(yz)^1(x^2-y^2)^1$ ($S = 2$) for the aqueous species into $(xy)^2(xz)^1(yz)^1$ ($S = 1$) for the two complexes with macrocyclic nitrogen donors.

The donor properties of the equatorial ligands have a strong influence on the Mössbauer parameters of these systems. Figure 9 shows experimental and calculated isomer shifts (see the Materials and Methods) for a collection of Fe^{III}, Fe^{IV}, and Fe^{V} compounds.[4,6,16,19,20] The overall cor-

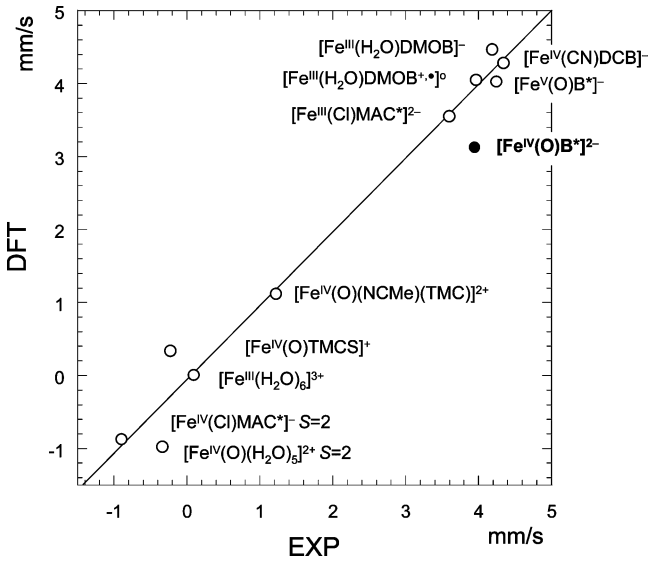

Figure 10. Correlation between DFT calculated and experimental quadrupole splittings for three different ligand systems.[4,6,19,20] The factor for the conversion of the quadrupole splitting from atomic units to mm/s is taken as -1.43 mm s^{-1}/AU to obtain a regression line with a slope of 1. Correlation coefficient R^2 is 0.96. Complex **2** is indicated with a solid dot.

relation between the experiment and theory is excellent. The isomer shift is a reliable indicator of the iron oxidation state in the comparison of complexes with similar equatorial ligands: $\delta(Fe^{III}) > \delta(Fe^{IV}) > \delta(Fe^{V})$. This trend is observed for all three ligand systems. For example, in the case of the TAML complexes, $\delta([Fe^{III}(Cl)MAC^*]^{2-}) = +0.25$ mm/s $> \delta([Fe^{IV}(Cl)MAC^*]^{-}) = -0.05$ mm/s and $\delta([Fe^{IV}(O)B^*]^{2-}) = -0.19$ mm/s $> \delta([Fe^{V}(O)B^*]^{-}) = -0.39$ mm/s. The removal of a 3d electron reduces the shielding of the iron nucleus and leads to a contraction of the occupied s orbitals, increasing the s electron density at the nucleus, and therefore, gives a lowering of the isomer shift.[42]

The isomer shifts of the Fe^{IV}=O species are dispersed over a remarkably broad range, from +0.39 to −0.19 mm/s, owing to the wide disparity in the donor capacities of the equatorial ligands. The effect of electron donation on δ depends upon the type of the acceptor orbital: thus, donation to a 3d orbital increases δ, whereas donation to 4s decreases the shift.[42] Because the 4s effect dominates,[29,35,43,44] there is a decrease in the isomer shift as a function of the increasing equatorial donor strength, e.g., $\delta([Fe^{IV}(O)(H_2O)_5]^{2+}) = +0.39$ mm/s $> \delta([Fe^{IV}(O)(NCMe)(TMC)]^{2+}) = +0.16$ mm/s $> \delta([Fe^{IV}(O)B^*]^{2-}) = -0.19$ mm/s. As a consequence, the Fe^{III}−TAML complexes in Figure 9 have δ values similar to those of the Fe^{IV} complexes with TMC and TMCS ligands, despite the difference in their formal oxidation states. The high-spin ($S = 2$) iron sites in $[Fe^{IV}(O)(H_2O)_5]^{2+}$ and $[Fe^{IV}(Cl)MAC^*]^{-}$ have substantially different isomer shifts (+0.39 versus −0.05 mm/s), showing that there is no unique relationship between the isomer shift and spin of Fe^{IV} sites.

The oxidation of $[Fe^{III}(H_2O)DMOB]^{-}$, where DMOB is the dimethoxy analogue of B*, is ligand-based and has virtually no effect on the isomer shift (see Figure 9). Conditions for ligand versus metal-based oxidation of TAML complexes have been discussed in ref 4.

3.4.3 Quadrupole Splitting ΔE_Q. Figure 10 displays the correlation between experimental and calculated quadrupole splittings, ΔE_Q.[4,6,16,19,20] Although the agreement is less satisfactory than in the case of the isomer shift, the calculations reproduce the marked trend in the dependence of ΔE_Q on ligand type. The systems in the right, upper corner of the figure are all TAML complexes. The large positive ΔE_Q values for these systems are due to the oblate (disk-shaped) charge distribution around the iron nucleus, arising from the large electronic charge donated by the N^{1-} amido groups into the x^2-y^2 orbital. The ΔE_Q values for the Fe^{III}−, Fe^{IV}−, and Fe^{V}−TAML complexes are remarkably similar. All Fe^{III} species have the $S = {}^3/_2$ configuration $(xy)^2(xz)^1(yz)^1(z^2)^1$, yielding a vanishing valence contribution to the quadrupole splitting, ∼0 mm/s, whereas the valence term of the $S = 1$ configuration $(xy)^2(xz)^1(yz)^1$ of the Fe^{IV} complexes contributes ∼ +4 mm/s. However, the large increase in the valence contribution to ΔE_Q caused by the removal of the z^2 electron is largely compensated by donation of electron density from the axial ligand into the vacated spin–orbital $(z^2)^\alpha$ and because the axial bonds of Fe^{IV} are stronger than those of Fe^{III}, by increased electron donations from the axial ligand(s) into $(xz)^\beta$, $(yz)^\beta$, and $(z^2)^\beta$, which are vacant in both the Fe^{III} and Fe^{IV} species (in this discussion, α is the spin of the electrons carrying the majority spin of the iron). The axial donations add up to a prolate (or spheroid generated by rotating an ellipse around its longer axis) charge distribution around the iron nucleus, contributing a negative term to ΔE_Q that nearly compensates the effect of the loss of the z^2 electron. In passing, we note that ΔE_Q, similar to δ, is hardly affected by the oxidation of the benzene moiety of the $[Fe^{III}(H_2O)DMOB]^{-}$ complex (Figure 10).

With the exception of $[Fe^{IV}(Cl)MAC^*]^{-}$, the TAML complexes in Figure 10 have larger ΔE_Q values than the non-TAML species, because TAMLs are substantially stronger σ donors. The MAC* complex differs from the other Fe^{IV}−TAML complexes in that the iron has the high spin ($S = 2$) configuration $(xy)^1(xz)^1(yz)^1(z^2)^1$.[45] The valence contribution (∼ −4 mm/s) of the MAC* species cancels almost completely against the large equatorial ligand contribution (∼ +3 mm/s), yielding a small net quadrupole splitting of ∼ −0.9 mm/s. $[Fe^{IV}(O)(H_2O)_5]^{2+}$ is also high-spin, but with orbital configuration $(xy)^1(xz)^1(yz)^1(x^2-y^2)^1$. Here, the valence contribution (∼ +4 mm/s) is compensated by the large, negative axial contribution to ΔE_Q of the oxo ligand, resulting in a small value for ΔE_Q.

3.4.4 Zero-Field Splitting, *g* Values, and Magnetic Hyperfine Coupling. On the basis of SCF calculations for the $S = 0$, 1, and 2 states of $[Fe^{IV}(O)B^*]^{2-}$ and the

(42) Walker, L. R.; Wertheim, G. K.; Jaccarino, V. *Phys. Rev. Lett.* **1961**, *6*, 98–101.
(43) McNab, T. K.; Micklitz, H.; Barrett, P. H. *Phys. Rev. B: Condens. Matter Mater. Phys.* **1971**, *4*, 3787–3797.
(44) Micklitz, H.; Litterst, F. J. *Phys. Rev. Lett.* **1974**, *33*, 480.
(45) Kostka, K. L.; Fox, B. G.; Hendrich, M. P.; Collins, T. J.; Rickard, C. E. F.; Wright, L. J.; Münck, E. *J. Am. Chem. Soc.* **1993**, *115*, 6746–6757.

application of TD DFT to the $S = 1$ ground state, we have estimated energies for both the spin-forbidden and spin-allowed d−d transitions of complex **2** (cf. Supporting Information). Through spin–orbit coupling, the excited states have a profound influence on the spectroscopic properties of the $S = 1$ ground multiplet.[13,14] In the Supporting Information, we present expressions for the zero-field splitting (D),[20] the deviation of the g values from the free-electron value (Δg), and a nonvanishing orbital term in the magnetic hyperfine coupling ($\mathbf{A}^{L}$). The expressions for D are similar but not identical[20,46] to those given in refs 13 and 14. The analysis adopted here takes into account covalency,[38] which causes a significant reduction in the value for D and related observables. The estimated value $D = 26.5$ cm^{-1} (see the Supporting Information) is in good agreement with the experimental data, $D = 24(3)$ cm^{-1}, and contains contributions for the three possible values of the spin of a d^4 system: $D = D_{S=0} + D_{S=1} + D_{S=2}$. The spin states contribute $D_{S=0} = +10.5$ cm^{-1}, $D_{S=1} = +10.8$ cm^{-1}, and $D_{S=2} = +5.2$ cm^{-1}, indicating that the contribution from excited $S \neq 1$ states is larger than those from $S = 1$ states. Taking the $S = 1$ ground configuration $\{xy^{\alpha}xy^{\beta}xz^{\alpha}yz^{\alpha}\}$ as a reference, $D_{S=0}$ can be assigned to the spin-forbidden transitions $xz^{\alpha} \rightarrow yz^{\beta}$ and $yz^{\alpha} \rightarrow xz^{\beta}$, $D_{S=1}$ to a predominant ($\sim$7 cm^{-1}) contribution from the spin-conserving transitions $xz^{\alpha} \rightarrow (z^2)^{\alpha}$ and $yz^{\alpha} \rightarrow (z^2)^{\alpha}$, and $D_{S=2}$ to the spin-forbidden transition $xy^{\beta} \rightarrow (x^2-y^2)^{\alpha}$.

In 1974, Oosterhuis and Lang[37] gave the crystal-field expressions for the zero-field splitting and the g and A tensors for the $S = 1$ ground multiplet of a $(t_{2g})^4$ configuration. The Oosterhuis and Lang (O−L) model considers spin–orbit coupling between the three $S = 1$ states generated when the β electron is placed into xy, yz, or xz. The O−L model is based on the assumption that the following interactions can be ignored: (i) spin–orbit coupling of the $S = 1$ ground state with $S \neq 1$ excited states and (ii) spin–orbit coupling of the ground state with $S = 1$ excitations to the e_g levels. Given the large "outer-spin-state" contributions to D (see above),[38] it is clear that condition (i) is violated in **2**. However, because the selection rule $\Delta S = 0$ for spin-independent interactions implies that spin–orbit coupling between multiplets of different spin has no first-order effect on the g values and the orbital contribution to the magnetic hyperfine tensor, the O−L model may still provide a good description for these quantities, unless condition (ii) is violated as well. The O−L expressions show that g_x and g_y increase as the t_{2g} crystal-field splittings decrease, so that $\Delta g_{\perp} = g_{\perp} - 2 > 0$. As we shall show below, this is not the case in **2**.

The magnetic hyperfine tensor is, in general, the sum of the Fermi-contact, spin-dipolar, and orbital terms: $\mathbf{A} = \mathbf{A}^{FC} + \mathbf{A}^{SD} + \mathbf{A}^{L}$. When spin–orbit coupling is treated in the second-order perturbation theory, the orbital contribution to the magnetic hyperfine tensor, $A^{L}_{\perp}$, is proportional to $P\Delta g_{\perp}$ (see Chapter 19 in ref 47), where $P = 2\beta g_n \beta_n \langle r^{-3} \rangle$. Thus, for $\Delta g_{\perp} > 0$, the orbital term opposes the (negative) Fermi-contact contribution and leads to a reduction in $A_{\perp}$. In our previous work on Fe^{IV}−TMC complexes,[20] we observed large D values ($D \approx 20$–35 cm^{-1}) as in the TAML complex, but without an apparent reduction in $A_{\perp}$. These observations indicated that the main contributions to D resulted from spin–orbit mixing of the $S = 1$ ground state with $S = 2$ and 0 excited states (see above).[13,14,20]

Our DFT calculations of $[Fe^{IV}(O)B^*]^{2-}$ suggest the presence of $S = 1$ excited states at $\sim$10 000 cm^{-1}, which result from xz, $yz \rightarrow z^2$ excitations (Table S1 in the Supporting Information). Mixing of these states with the $S = 1$ ground state produces a $\Delta g_{\perp} < 0$ and thus a negative contribution to $A_{\perp}$. Our calculations, described in sections S1−S3 in the Supporting Information, suggest that $\Delta g_{\perp} = -0.04$ and $g_{\perp} = 1.96$ for $[Fe^{IV}(O)B^*]^{2-}$. Thus, condition (ii) of the O−L model is not fulfilled either in **2** [As worked out in the seminal paper of Neese and Solomon,[38] the signs of the contributions to $\Delta g_{\perp}$ and $A^{L}_{\perp}$ (eq S7 in the Supporting Information) depend upon the occupation numbers of the initial and final orbital states of the excited electron: a (half-filled → empty transition) gives a negative term and a (filled → half-filled) transition yields a positive term (cf. eq S7 in the Supporting Information)]. This effect might explain why the experimental A_x and A_y values are ca. 2–3 T larger in magnitude than those observed previously for Fe^{IV}=O complexes.[3]

The principal axes of $\mathbf{A}^{SD}$ and $\mathbf{A}^{L}$ in $[Fe^{IV}(O)B^*]^{2-}$ coincide with the x, y, and z axes (Figure 8) used in the discussion of the 3d orbitals (NB the principal axes in the $x-y$ plane are defined apart from a rotation because of eigenvalue degeneracy). For the optimized geometry of Figure 8, our DFT calculations for the spin-dipolar term yield the components $\mathbf{A}^{SD} = (-7, -7, \text{and } +14)$ T. A calculation for the $|xy^{\alpha}xy^{\beta}xz^{\alpha}yz^{\alpha}|$ ground state gives $\mathbf{A}^{SD} = (-^1/_7, -^1/_7, \text{and } +^2/_7)P$, yielding $P = 49$ T, in excellent agreement with the empirical value $P = 50$ T that we have used for Fe^{IV}−TMC complexes in earlier work.[20] Using the DFT values obtained for P together with $\Delta g_{\perp} = -0.04$ and $\Delta g_z = 0$ yields for the orbital term $\mathbf{A}^{L} = (-2, -2, \text{and } 0)$ T. The isotropic part of the A tensor $A^{iso} = (A_x + A_y + A_z)/3$ comprises the Fermi-contact contribution and a small orbital (pseudo-contact) contribution $A^{L,iso} = P\Delta g_{av} = -1.3$ T, where $\Delta g_{av} = g_{av} - 2$ and $g_{av} = (g_x + g_y + g_z)/3$. For complex **2**, we have $A^{iso}(\text{exp}) = -17.3$ T, yielding $A^{FC}(\text{exp}) = -16$ T. The contact term is generally poorly described by DFT (a correction factor of 1.8 has been suggested in ref 18). The contact term is often expressed as $A^{FC} = \kappa P$, yielding $\kappa \approx 0.33$. Summing the three contributions yields $\mathbf{A} = \mathbf{A}^{FC} + \mathbf{A}^{SD} + \mathbf{A}^{L} \approx (-25, -25, \text{and } -2)$ T, which describes well the two large negative components along x and y and the nearly vanishing component along z. The contact term is a measure of the spin delocalization of the metal site. In this context, it is interesting to note that $[Fe^{V}(O)B^*]^{-}$ has $A^{FC} = -18$ T, indicating some degree of spin polarization of the electron density donated by oxygen into the vacated xzorbital.

3.4.5 Comparison of 2 with Other Nonheme Iron(IV)−Oxo Complexes. The $S = 2$ ground configuration of $[Fe^{IV}(O)(H_2O)_5]^{2+}$ (see section 3.4.3) and the $S = 1$ ground

(46) We find different values for some of the numerical factors.

Table 4. Comparison of Parameters for $[Fe^{IV}(O)B^*]^{2-}$ and $[Fe^{IV}(O)(NCMe)TMC]^{2+}$[48]

	TAML	TMC
$Fe-N_{eq}$[a] (Å)	1.90[b]	2.09[b]
Fe−O (Å)	1.69	1.65
δ (mm/s)	−0.19	+0.17
ΔE_Q (mm/s)	+3.95	+1.23
$A_\perp$ (T)	−27.0	−22.5
D (cm^{-1})	+24	+29

[a] eq = equatorial. [b] Averages.

configurations of $[Fe^{IV}(O)B^*]^{2-}$ and $[Fe^{IV}(O)(NCMe)(TMC)]^{2+}$ are interchangeable by the spin-forbidden transitions $xy^\beta \leftrightarrow (x^2-y^2)^\alpha$. The spin–orbit coupling between these two states has been proposed as the principal mechanism for generating the zero-field splittings in both $[Fe^{IV}(O)(H_2O)_5]^{2+}$ ($D = 9$ cm^{-1}) and $[Fe^{IV}(O)(NCMe)(TMC)]^{2+}$ ($D = 29$ cm^{-1}) (see refs 13, 16, 19, and 20). However, this mechanism furnishes only a secondary contribution to D in $[Fe^{IV}(O)B^*]^{2-}$ (see section 3.4.4). The difference between the two $S = 1$ species can be explained as follows. As shown in Table 4, the Fe−N distances in the TAML species are shorter than in the TMC species. As a consequence, the energy of the spin-forbidden $xy \rightarrow x^2-y^2$ transition to the $S = 2$ excited state in the TAML species is higher than in the TMC species, leading to a smaller value for $D_{S=2}$ for the TAML species (see section 3.4.4). However, the smaller value for $D_{S=2}$ is partially off-set by a larger value for $D_{S=1}$ in the TAML species: because the Fe−O distance in the TAML species is longer than in the TMC species (Table 4), the xz, $yz \rightarrow z^2$ energy is lower, and the associated value for $D_{S=1}$ (see section section 3.4.4) is therefore higher than for the TMC complex, leading altogether to a slightly smaller value for D (Table 4). The values for the hyperfine parameters in Table 4 corroborate the larger ligand strength of TAMLs relative to TMC: the B* complex has a smaller δ value than the TMC complex because of increased charge donation into the 4s orbital (see section 3.4.2), a larger ΔE_Q value resulting from an increased in-plane and reduced axial electron donation (see section 3.4.3), and a smaller $A_\perp$ value (see section 3.4.4) originating from the increase in the orbital angular momentum in the x, y plane attending the increase in $D_{S=1}$ (see above).

The Fermi-contact terms for $[Fe^{IV}(O)(H_2O)_5]^{2+}$ ($A^{FC} = -25$ T, ref 19), $[Fe^{IV}(O)(NCMe)(TMC)]^{2+}$ ($A^{FC} = -15$ T, refs 16 and 20), and $[Fe^{IV}(O)B^*]^{2-}$ ($A^{FC} = -16$ T) imply contributions to the internal field of −12.5, −7.5, and −8 T/unpaired electron, respectively. These values indicate that the delocalization of the iron spin onto the ligands in the TMC and TAML species is significantly larger than in the aqueous complex.

In conclusion, the differences in the fine- and hyperfine-structure parameters for the TAML and TMC species in Table 4 are a consequence of the strong donor properties of the TAML and support the identification of **2** as a $[Fe^{IV}(O)TAML]^{2-}$ complex.

Acknowledgment. The work was supported by National Institutes of Health (NIH) Grants EB-001475 (E.M.) and GM-38767 (L.Q.), the Heinz Endowments (T.J.C.), and Environmental Protection Agency (EPA) (Grant RD 83 to T.J.C.). XAS data were collected on beamline 9-3 at the Stanford Synchrotron Radiation Laboratory (SSRL). The SSRL Structural Molecular Biology Program is supported by the Department of Energy, Office of Biological and Environmental Research, and the National Institutes of Health, National Center for Research Resources, Biomedical Technology Program.

Supporting Information Available: Figure S1, Tables S1–S3, and details on fine structure and hyperfine parameters. This material is available free of charge via the Internet at http://pubs.acs.org.

IC7022902

(47) Abragam, A.; Bleaney, B. *Electron Paramagnetic Resonance of Transition Ions (International Series of Monographs on Physics)*; Dover: New York, 1970; Vol. Chapter 19, p 912.
(48) Costas, M.; Rohde, J.-U.; Stubna, A.; Ho, R. Y. N.; Quaroni, L.; Münck, E.; Que, L., Jr. *J. Am. Chem. Soc.* **2001**, *123*, 12931–12932.